Self-interacting scalar field distributions around Schwarzschild black holes

Alejandro Aguilar-Nieto,[1] Víctor Jaramillo,[1] Juan Barranco,[2] Argelia Bernal,[2] Juan Carlos Degollado,[3] and Darío Núñez[1]

[1]*Instituto de Ciencias Nucleares, Universidad Nacional Autónoma de México, Circuito Exterior C.U., A.P. 70-543, México D.F. 04510, Mexico*

[2]*Departamento de Física, División de Ciencias e Ingenierías, Campus León, Universidad de Guanajuato, León 37150, Mexico*

[3]*Instituto de Ciencias Físicas, Universidad Nacional Autónoma de México, Apartado Postal 48-3, 62251, Cuernavaca, Morelos, Mexico*

(Received 29 November 2022; accepted 31 January 2023; published 27 February 2023)

Long-lived configurations of massive scalar fields around black holes may form if the coupling between the mass of the scalar field and the mass of the black hole is very small. In this work we analyze the effect of self-interaction in the distribution of the long-lived cloud surrounding a static black hole. We consider both attractive and repulsive self-interactions. By solving numerically the Klein-Gordon equation on a fixed background in the frequency domain, we find that the spatial distribution of quasistationary states may be larger as compared to the noninteracting case. We performed a time evolution to determine the effect of the self-interaction on the lifetime of the configurations our findings indicate that the contribution of the self-interaction is subdominant.

DOI: 10.1103/PhysRevD.107.044070

I. INTRODUCTION

Scalar fields are promising candidates to explain the nature of dark matter. In a scalar-field dark matter model it is assumed that a classical field makes up the main fraction of the dark matter of the Universe. The description relies on the fact that a coherently, weakly-interacting, oscillating light scalar field formed a Bose-Einstein condensate (BEC) in a nonrelativistic and low-momentum state [1–8]. The BEC has a phase space density that enables it to describe the density profile of the galactic dark matter halo for a convenient approximations. Amongst the many proposed candidates, axions, particles introduced by Peccei and Quinn [9], are scalar fields with a nonzero vacuum expectation value and keep the CP invariance of the strong interactions in the Lagrangian involving all Yukawa couplings. The effects of such scalar field and other axionlike particles (with a lower mass) in astrophysical and cosmological scenarios have been investigated extensively; see, e.g., Refs. [10–19].

Since the detection of gravitational waves by the LIGO-Virgo-Kagra Collaboration [20–23] and the recent developments in electromagnetic observations, in particular the image of the central black hole and its shadow of M87 and Sagittarius A* captured by the Event Horizon Telescope [24–26], there is a renewed interest in the physical processes that may occur in the vicinity of compact objects.

Massive bosonic fields may form quasibound states around a black holes [27–33]. In a Schwarzschild background, all of these states are unstable and decay, leaking part of the field towards the black hole [34,35]. These scalar configurations are characterized by instability timescales which are much longer than the timescale set by the mass of the central black hole. Because of the low rate of decay, the scalar field configurations may remain surrounding a black hole for large timescales depending on the values of the parameters involved [36]. Therefore, scalar fields around black holes represent a very convenient setup which model a supermassive black hole surrounded by a dark matter halo in galaxies. Quasistationary solutions to the Klein-Gordon equation on a Schwarzschild background in that context, were described in detail by Barranco *et al.* in Refs. [36–38]. The results obtained in those references, indicate that it is possible that scalar field halos may last for cosmological timescales around supermassive black holes. These long-lived configurations composed of a complex, massive and nonself-interacting scalar field, were found to be characterized essentially by two parameters, namely the integer ℓ, associated with the angular distribution of the field and the dimensionless quantity formed by the mass coupling between the mass of the black hole M, and the mass of the scalar particle m, $GMm/\hbar c$, which can also be interpreted as one half of the ratio between the black hole horizon radius $r_h = 2GM/c^2$ and the characteristic wavelength of the scalar field $\lambda_\phi = \hbar c/m$.

For a scalar particle, the simplest nongravitational interaction is a quartic self-interaction. This generalization can be achieved by expanding a potential about a symmetric minimum, and realizing that the quartic term is the most important interaction term for small amplitudes.

From the point of view of a field theory the quartic self-interaction is the largest value in the exponent that allows a renormalizable theory. In an astrophysical scenario, Colpi *et al.* [39] showed that self-interactions in boson stars can produce significant phenomenological changes. In particular, they show that the upper limit on the mass of boson stars increases notably compared to the noninteracting case. Such findings show that boson stars can have masses even larger than a solar mass. Furthermore, in some regimes self-interacting boson stars are compact enough to be considered black hole mimickers [40–45]. From a cosmological perspective, the role of self-interaction is of great importance in dark matter models, particularly within complex scalar field models as in Refs. [46,47] where it has been shown that with a repulsive self-interaction, the scalar field goes through a radiationlike stage in the Friedman evolution which in turn increases the effective number of relativistic degrees of freedom that matches the estimates of big bang nucleosynthesis (see also [48] for further discussion).

Quasistationary states of attracting self-interacting scalar fields where found in the context of gravitational collapse of unstable boson stars in Ref. [49]. The evolution of self-interacting boson stars in spherical symmetry was performed by solving the Einstein-Klein-Gordon system numerically. When describing an unstable configuration, boson stars collapsed forming a black hole surrounded by a remnant of scalar field leaving long-lasting states around the newly formed black hole.

In this work, we solve the Klein-Gordon equation describing a self-interacting scalar field in the background of a Schwarzschild black hole. We assume the field oscillates coherently and analyze the system in the frequency domain to find resonant states. We analyze in detail the consequences of a quartic self-interaction in the distribution of the field and present a thorough analysis of the quasistationary solutions. We observe that the self-coupling have important consequences in the phenomenology associated with scalar field distributions. We further analyze the behavior in time of the scalar distribution.

The paper is organized as follows: In Sec. II we present the formulation, the background spacetime, and method of construction of the solutions. In Sec. III we present some examples of solutions of the Klein-Gordon equation and describe the properties of resonant modes. In Sec. IV we discuss the time development of resonant modes. Finally, we summarize our results and present concluding remarks in Sec. V. Throughout the paper we use geometric units such that $c = 1 = G$.

II. SETUP

In this work, we will focus on the regime where self-interaction effects on the field become significant before gravitational backreaction and therefore, we shall restrict this analysis to a fixed black hole spacetime. We consider a complex massive scalar field Φ with mass m described by the action $S = -\int d^4x\sqrt{-g}[\nabla^\sigma\Phi^*\nabla_\sigma\Phi + V(|\Phi|)]$ with

$$V(|\Phi|) = \mu^2|\Phi|^2 + \frac{1}{2}\eta\lambda|\Phi|^4. \tag{1}$$

where $\mu = m/\hbar$ and for convenience we consider $\lambda > 0$. The attractive or repulsive nature of the self-interaction is set by $\eta = 1$ or $\eta = -1$, respectively.

The stress-energy tensor of the scalar field reads

$$T_{\alpha\beta} = \frac{1}{2}(\nabla_\alpha\Phi\nabla_\beta\Phi^* + \nabla_\beta\Phi\nabla_\alpha\Phi^* - g_{\alpha\beta}[\nabla^\sigma\Phi\nabla_\sigma\Phi^* + V(|\Phi|)]). \tag{2}$$

The conservation of the stress-energy tensor $\nabla_\nu T^{\mu\nu} = 0$ provides the corresponding equation of motion for the field, the Klein-Gordon equation,

$$\nabla_\alpha\nabla^\alpha\Phi = \frac{dV(|\Phi|)}{d\Phi^*}, \tag{3}$$

and its complex conjugate. We consider the background spacetime as the nonrotating Schwarzschild black hole in Boyer-Lindquist coordinates (t, r, θ, φ) with element of line given by

$$ds^2 = -N(r)dt^2 + N^{-1}(r)dr^2 + r^2d\Omega^2, \tag{4}$$

with $N(r) = 1–2M/r$, and $d\Omega^2 = d\theta^2 + \sin^2\theta d\varphi^2$. We assume that the scalar field is spherically symmetric and thus can be written as

$$\Phi(t, r) = \frac{u(r)}{r}e^{i\omega t}, \tag{5}$$

where ω is a real number. The resulting Klein-Gordon equation takes the form

$$\left[-N(r)\frac{d}{dr}\left(N(r)\frac{d}{dr}\right) + N(r)\mathcal{U}(r)\right]u(r) = \omega^2u(r), \tag{6}$$

where

$$\mathcal{U}(r) = \frac{2M}{r^3} + \mu^2 + \eta\lambda\frac{u^2(r)}{r^2}. \tag{7}$$

We will use the fact that the static spacetime at hand has a timelike Killing vector to define a diagnostic quantity with respect to the stress energy of the system. The energy density of the scalar field measured by a static observer, $\rho = -T_0{}^0$, provides a useful measure of the distribution of the field in the spacetime, explicitly is given as

$$\rho = \frac{1}{2r^2}\left(\frac{\omega^2u^2}{N} + N\left(\frac{du}{dr}\right)^2 + \mathcal{U}(r)u^2 - \frac{d}{dr}\frac{Nu^2}{r}\right). \tag{8}$$

This quantity will be used to characterize the scalar field distribution in the following sections. Another quantity of interest is the total mass-energy stored by the scalar field obtained by the integration of the energy density

$$M_\Phi = 4\pi \int_{2M}^{\infty} \rho r^2 dr. \tag{9}$$

This quantity gives an estimation of the amount of scalar field in the spacetime that can be compared with the mass of the black hole.

A. Scaling properties

In order to explore the space of solutions of the Klein Gordon equation (6), we define a new function $v(r)$ as

$$v(r) = \sqrt{\lambda} u(r), \tag{10}$$

such that the function $\mathcal{U}(r)$ becomes

$$\mathcal{U}(r) = \frac{2M}{r^3} + \mu^2 + \eta \frac{v^2(r)}{r^2}. \tag{11}$$

The function v encodes the self-interaction parameter and allow us to explore the solution space of Eq. (6) providing an infinite set of solutions for each value of λ. Additionally, in order to better resolve the behavior of the field in the region close to the horizon, we use the tortoise coordinate, $r^* = r + 2M \ln(r/2M - 1)$, to rewrite Eq. (6) as

$$-\frac{d^2 v}{dr^{*2}} + N(r)\mathcal{U}(r)v = \omega^2 v, \tag{12}$$

where r is given implicitly in the definition of r^*. One can thus eliminate λ from the numerical task because it always appears as a scalar. Equation (12), poses a further rescaling property, which is specified in Table I. This rescaling allows us to use dimensionless quantities such as r/M, $M\mu$, $M\omega$, etc., to specify any quantity in terms of the mass of the black hole. The dependence on the parameters in the Klein-Gordon equation is in $M\mu$, and the value of η (which is $+1$ or -1).

B. Asymptotically decaying solutions

Equation (12) represent a nonlinear eingenvalue problem for the function v and eigenvalue ω. Before presenting its solutions and the methods we employed to solve it, let us first emphasize some of the properties of the solution. In the near horizon region $r^* \to -\infty$, the function $N(r) \to 0$, consequently solutions of Eq. (12) may have the form

$$v(r^*) \approx A\cos(\omega r^* - \delta), \tag{13}$$

where the amplitude A and the phase δ are real numbers. Notice however, that the function (13) together with the ansatz (5), contains no physical solutions since it represents both outcoming and ingoing modes. The physical situation we shall consider, a field distribution around a black hole, excludes outgoing modes. In the following section we will address this issue in more detail.

Let us consider values of ω such that $\omega < \mu$. Then, in the limit $r^* \to \infty$, Eq. (12) admits exponentially decaying or growing solutions of the form $v(r^*) \approx C\exp(-kr^*) + D\exp(+kr^*)$ with $k = \sqrt{\mu^2 - \omega^2}$. Since we are interested in describing localized solutions, consistent with the asymptotically flat metric, we will focus on the solutions with exponential decay and set $D = 0$.

The previous descriptions concerns only the asymptotic behavior of the solutions of Eq. (12). With only this information, the possible values that ω can take are infinite and the spectra is continuous.

In the next section we shall show that there is a set of discrete values of ω that allows solutions with a much larger amplitude far outside the horizon compared to the amplitude of the field near the horizon. These solutions are thus closer to the physical description of having an event horizon as the left boundary.

In order to find the solutions of Eq. (12) we integrate it numerically as follows. We fix η, and μ and choose some value ω which in turn fixes k. Then we choose a value of v

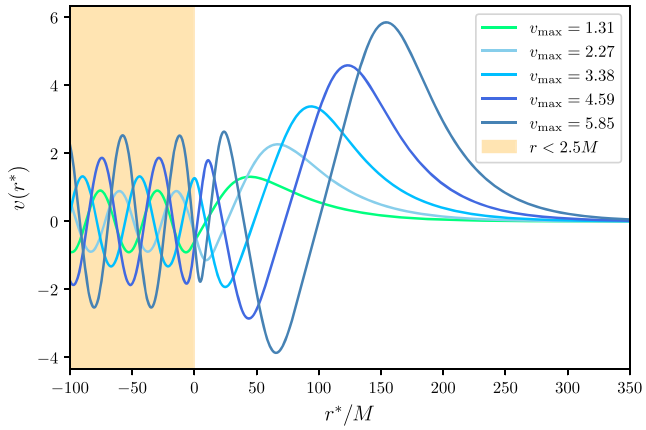

FIG. 1. Sample of solutions of Eq. (12) with an exponential decay at infinity. In the region close the horizon (shaded area, $r* \to -\infty$) solutions behave according to Eq. (13), the maximal amplitude in this region sets the value of A. The value in the far region set by the C also fixes the value of $v_{\max}$. Thus, each solution can be characterized by the amplitudes A and $v_{\max}$.

TABLE I. Rescaling properties of the Klein-Gordon equation in the Schwazschild background [Eq. (6)].

$M \mapsto \alpha M$
$r \mapsto \alpha r$
$(\mu, \omega) \mapsto \alpha^{-1}(\mu, \omega)$
$(u, \lambda) \mapsto (u, \lambda)$

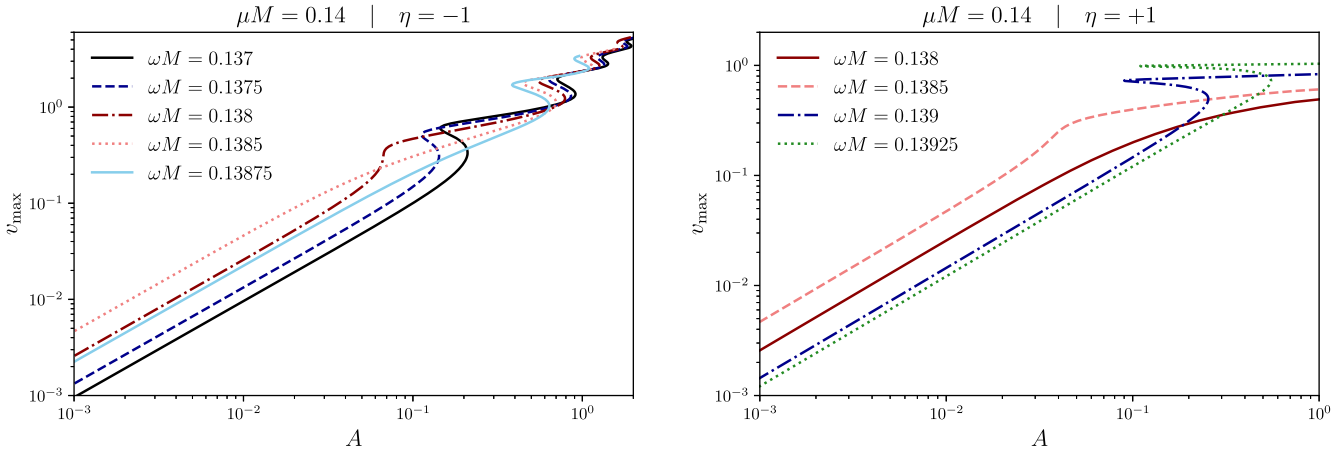

FIG. 2. Amplitude near the horizon A, and $v_{\max}$, for solutions of Eq. (12). Each point of the curve characterizes an asymptotically decaying solution with a behavior close the horizon given by Eq. (13). Without specifying the boundary conditions the spectra in ω is a continuum. The weak self-interacting regime corresponds to the extreme left in both panels, where the behavior is almost linear.

at the outermost point of the numerical grid $r^*{}_{\max}$ and obtain the corresponding value of the derivative dv/dr^* at that point, as $dv/dr^*|_{r^*_{\max}} = -kv|_{r^*_{\max}}$, and once this pair of conditions is set, we integrate the second-order differential equation inwards up to the left boundary $r^*{}_{\min}$. Figure 1 shows the plot of v for $M\mu = 0.14$ and $M\omega = 0.1370$ obtained by this procedure. There is a region in which the behavior of Eq. (13) is reached and the function v is completely characterized by its amplitude A. Furthermore, we have found that for each solution $v(r)$, the quantity $v_{\max}$, defined as the local maximum attained by the function v in the far horizon region, can be used to characterize that solution. In the next section we will show that comparing the amplitude in the far region, $v_{\max}$, with the amplitude near the horizon A, it is possible to find a discrete set of values of ω that allows quasibound or resonant configurations.

Decaying solution are characterized by the amplitudes A and $v_{\max}$ for a given value of ω. Figure 2 displays sets of solutions with the desired asymptotic behavior for some values of ω. We will refer solutions with $v_{\max} \to 0$ as solutions in the *weak self-interacting regime*. As the value of $v_{\max}$ increases, the term v^2 in Eq. (12) becomes important and defines solutions in the *strong self-interacting regime*. These functions however, are not physical in the sense that we have not yet imposed the boundary condition at the left. That is, these functions contain outgoing modes coming from the left which is not physically possible.

III. RESONANT STATES

It is possible to quantify the amount of the scalar field that accumulates in the outer region with respect to the amplitude near the horizon by comparing the values of $v_{\max}$ and A. In Fig. 3 we show a projection map of the ratio $A/v_{\max}$, which reaches a minimum whenever the amount of scalar field in the external region is maximal with respect to the region close to the horizon using several values of ωM for $\mu M = 0.14$. This value allows us to select the solutions with the lowest ratio as quasiresonant solution. In this way, the behavior of the field given by Eq. (13) can be neglected for some solutions which we select as quasiresonant modes since its amplitude is much smaller than the amplitude far outside the horizon. The left panel corresponds to $\eta = -1$ and the right panel corresponds to $\eta = 1$. In order to better visualize the frequencies of the resonant states and get some understanding on their change in $v_{\max}$, Fig. 4 shows constant $v_{\max}$ cuts of the projected surface in Fig. 3. In these plots, resonant states are those solutions (represented by each curve) whose ratio $A/v_{\max}$ has a minimum.[1] The value of the frequency at which the first minimum occurs corresponds to the frequency of the first resonant state (higher frequencies have been called overtones in close analogy to harmonic frequencies). Consequently, configurations surrounding a static black hole with a larger amplitude far from the event horizon are characterized by a discrete set of frequencies ω. These modes for $\lambda = 0$ have been already characterized in Ref. [36]. The effect of the self-interaction in the resonant states is to induce a change in the values of the frequencies as can be seen in Fig. 3. The frequency of the resonant states in the limit $v_{\max}$ through the vertical bands in Figs. 3 match the value of the fundamental and first resonant frequencies $M\omega = 0.13837$ and $M\omega = 0.13956$, respectively, for $M\mu = 0.14$ and $\lambda = 0$. For $\eta = -1$, as $v_{\max}$ increases the frequencies of the resonant states decrease with respect to the noninteracting case, while for $\eta = +1$ the frequencies increase.

[1]We have verified that the characterization of resonant state, using the quantity $A/v_{\max}$, leads to a discrete set of frequencies in the $\lambda \to 0$ limit, which is consistent with the resonant modes given in Ref. [36].

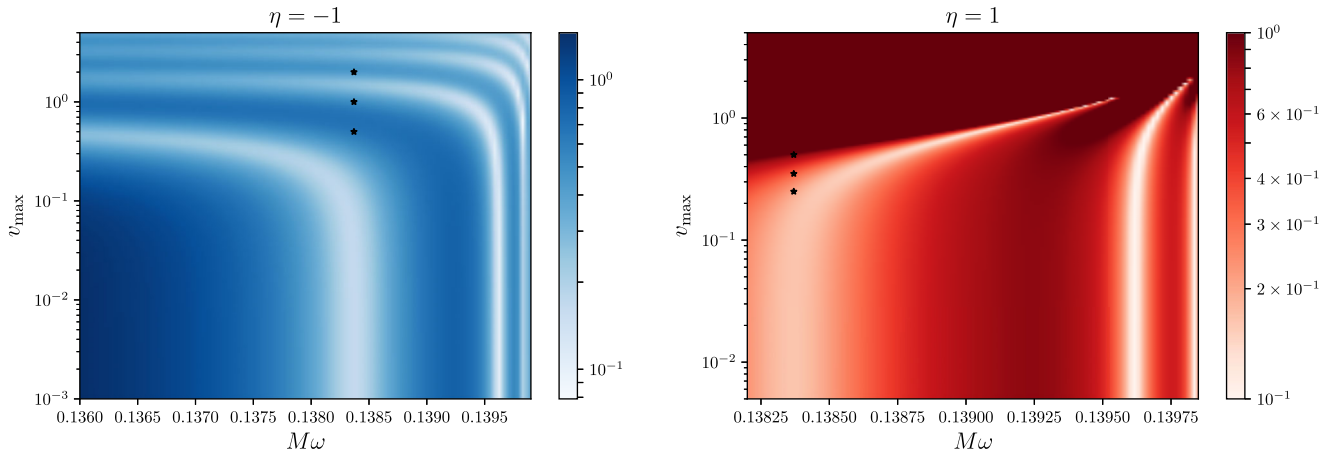

FIG. 3. Color map of the ratio $A/v_{\max}$ for $M\mu = 0.14$. The intensity of the color indicates the value of the ratio. The white bands, in which the value of $v_{\max}$ is much larger than A, correspond to resonant states. The left panel is for $\eta = -1$ and right panel is for $\eta = +1$. The weakly self-interacting regime correspond to the lower part in which $v_{\max} \to 0$. For larger values of $v_{\max}$ solutions can not be found for $\eta = +1$. The asterisk symbols are the configurations of Figs. 6 and 7 with frequency $\omega = 0.13837$.

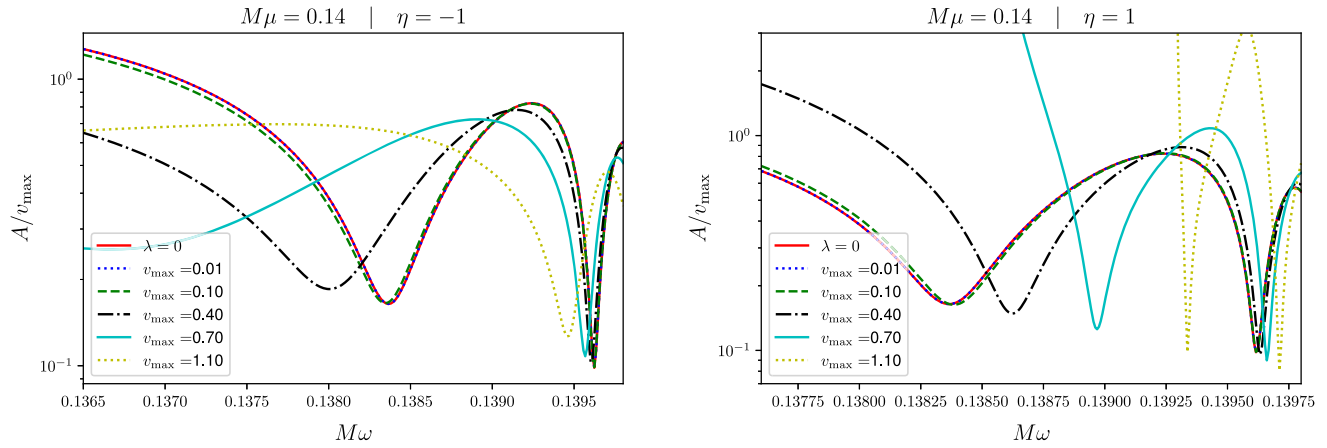

FIG. 4. Ratio $A/v_{\max}$ as a function of ω for different values of $v_{\max}$ and $M\mu = 0.14$ The local minima on each curve denote resonant solutions. The case with $\lambda = 0$ is also shown as a reference. In the weak regime the curves are almost indistinguishable from the noninteracting case.

Fundamental frequencies of resonant states are shown in Fig. 5 as a function of $v_{\max}$ for some representative values of $M\mu$. We have found that for $\eta = +1$ there might be no resonant states with higher values of $v_{\max}$. Other results related to the scalar field distribution as well as the issue about the lifetime of these states will be addressed below.

A. Properties of resonant states

As stated before, the effect of the magnitude of λ on the radial profile of the scalar field can be described in terms of $v_{\max}$. The first scenario we examine is the one where $\eta = -1$ and ω is fixed and compare nonresonant self-interacting solutions with the first resonant state in the $\lambda \to 0$ case. As a particular example, by taking the frequency $M\omega = 0.13837$ (that corresponds to the first resonant state with $\lambda = 0$ and $M\mu = 0.14$), configurations in the weak self-interacting regime are almost indistinguishable from the case with $\lambda = 0$. In the strong regime the profiles differ slightly because these configurations are no longer resonant states. Figure 6 displays the profiles $v(r^*)$ and the radial energy density $\rho_e = 4\pi r^2 \rho$, with $\eta = -1$, $M\mu = 0.14$, and a fixed frequency $M\omega = 0.13837$ for some representative values of $v_{\max}$ in both weak and strong self-interacting regimes, the case with $\lambda = 0$ is also shown for comparison. The configurations in Fig. 6 correspond to the asterisk symbols in Fig. 3. For large values of $v_{\max}$, the ratio $A/v_{\max}$ becomes larger and it may happen that for large enough values of $v_{\max}$ along the fixed frequency, a profile with one or more nodes is found. Like in the $\lambda = 0$ case, overtones correspond to solutions with increasing number of nodes as ω approaches μ. In the negative self-interaction case, $\eta = -1$, the effect of increasing λ in the mass density is that the scalar field distribution spreads over a larger region and the

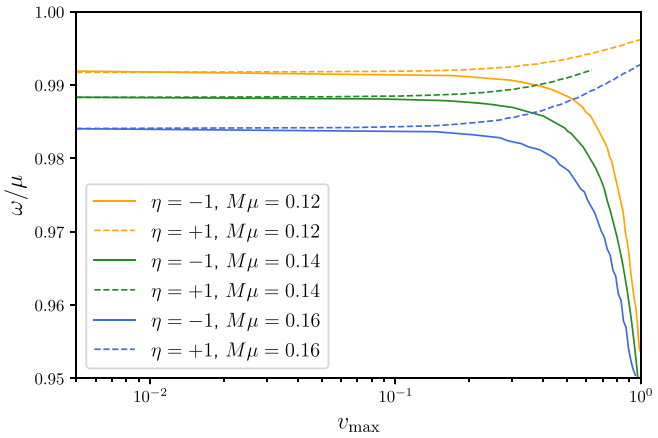

FIG. 5. Fundamental frequencies of resonant states, as a function of $v_{\max}$ for several cases of $M\mu$ for both, positive and negative self-interaction. For $\eta = +1$ (dashed line), as $v_{\max}$ grows, there are no resonant states.

maximum moves away from the horizon. The normalized mass density is shown in the right panel of Fig. 6. Given the behavior in Eq. (13), solutions of Eq. (12) produce an infinite energy density at the horizon. A positive self-interaction $\eta = +1$ produces analogous changes in the radial profile of the scalar field; in this case however, the field concentrates closer the horizon and the changes are smaller in magnitude. Another important difference is that for large values of $v_{\max}$ resonant solutions cease to exist. Figure 7 displays the radial scalar field profile and the radial energy density for $\eta = +1$.

In the following we shall focus on the fundamental resonant states as $v_{\max}$ increases. Figure 8 shows the scalar-field profile of the fundamental resonant state for both $\eta = -1$ and $\eta = +1$. Each resonant state is characterized by its frequency and $v_{\max}$. As $v_{\max}$ increases the amplitude of the radial profile $v(r)$ increases for both $\eta = -1$ and $\eta = +1$. The radial density presents the same behavior as is displayed in Fig. 9. For $\eta = +1$ the effective size of the configuration increases in the strong-interacting regime. Another important effect of the self-interaction on the distribution of the scalar field is in the mass of the configuration. Self-interacting configurations are heavier than their noninteracting partners. In the weak self-interacting regime, the mass increases almost linearly with $v_{\max}$ for both $\eta = -1$ and $\eta = +1$. In the strong regime however, the growth slows down for $\eta = -1$. Figure 10 shows the mass M_Φ as a function of $v_{\max}$ for some values of the gravitational coupling $M\mu$ considering $\eta - 1$ and $\eta = +1$.

In the nonself-interacting case, an effective potential of the time-independent Schrödinger-like equation (12) (with $\lambda = 0$) can be defined. In the self-interacting case, such effective potential has the form

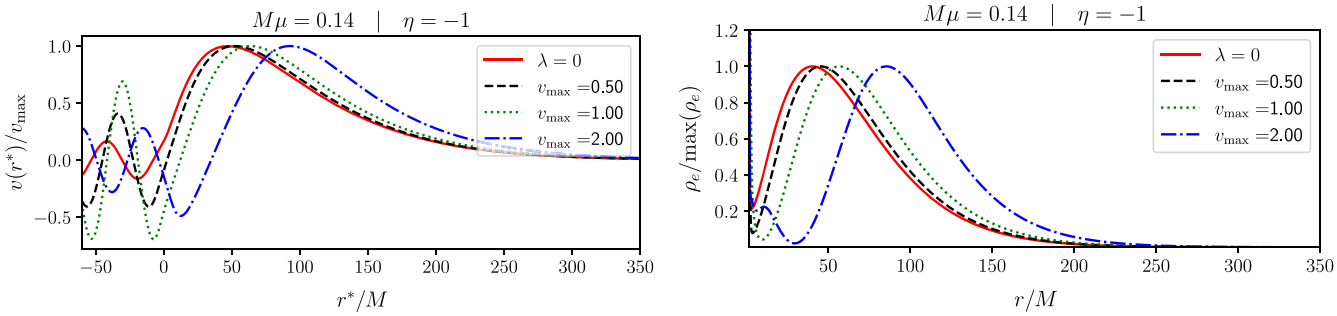

FIG. 6. The left panel shows the profile of the scalar field and the right panel the corresponding radial energy density for a fixed value of $M\omega = 0.13837$ with different values of $v_{\max}$. The case $\lambda = 0$ is included for comparison. Both sets have been normalized for a better visualization.

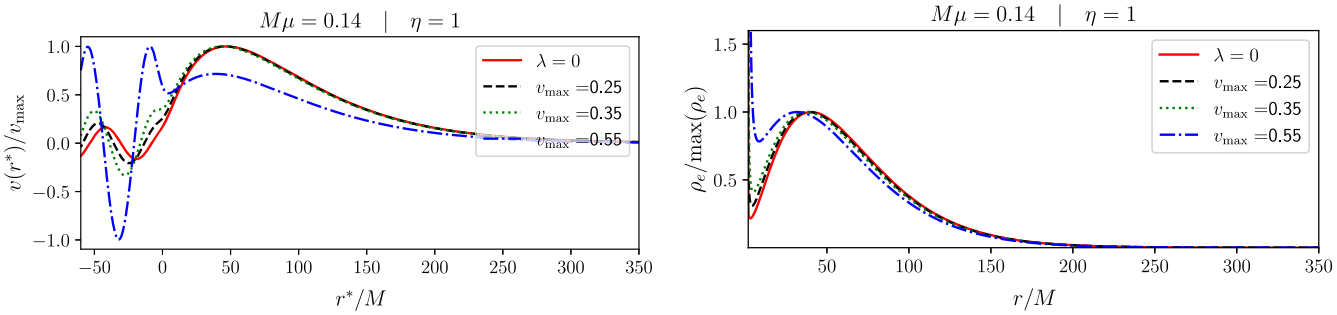

FIG. 7. Same as Fig. 6 with $\eta = 1$.

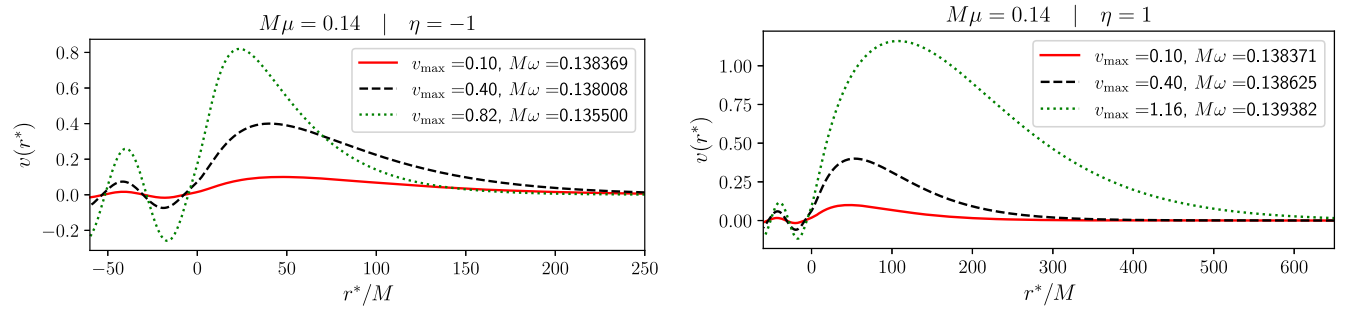

FIG. 8. Scalar-field profile for the first resonant state for different values of $v_{\max}$ for $\eta = -1$, left panel, and $\eta = +1$, right panel.

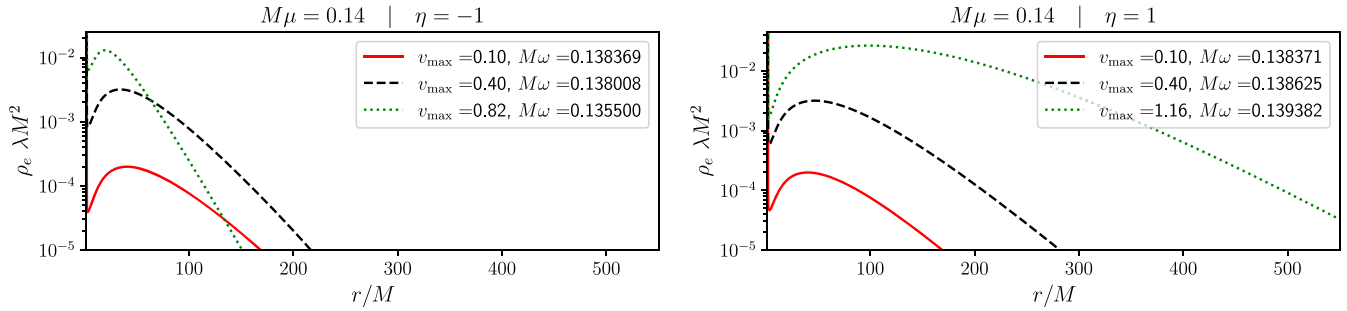

FIG. 9. Radial energy density for the first resonant states for different values of $v_{\max}$. Left panel correspond to $\eta = -1$ whereas right panel corresponds to $\eta = +1$. For $\eta = +1$ the characteristic size of the boson cloud in the strong self-interacting regime is much larger than the size of the cloud in the weak self-interacting regime.

$$V_{\rm eff}(r) = N(r)\left(\frac{2M}{r^3} + \mu^2 + \eta\lambda\frac{u^2(r)}{r^2}\right). \tag{14}$$

The effective potential interpretation may help in the characterization of the solutions (see [36,37] and references therein) however, for $\lambda \neq 0$, $V_{\rm eff}$ can only be obtained *a posteriori* since the knowledge of $v(r)$ [and consequently $u(r)$] is required. In any case, the effective potential may be useful to determine the resonance band formed by the parameters $M\mu$ and $M\omega$ for which the solutions have the possibility of being concentrated as shown in Fig. 11. The existence of the potential well in the $\lambda = 0$ case is granted by the condition $M\mu < 1/4$ [36]. However, a similar bound cannot be found for $\lambda \neq 0$.

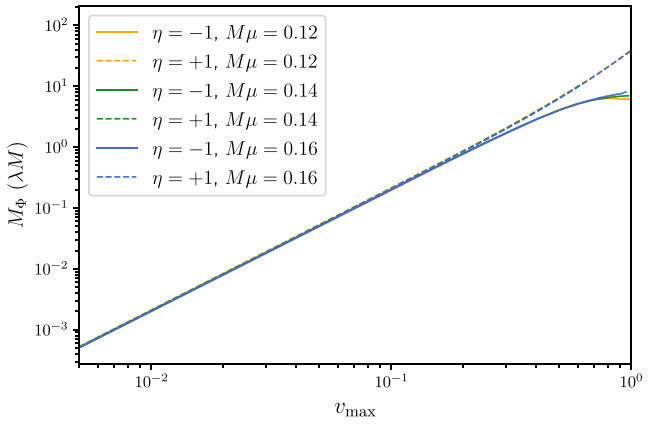

FIG. 10. Mass of the scalar field as defined by Eq. (9). In order to avoid the divergence produced by the oscillatory behavior at the horizon, the integration was performed from $r = 2M + \epsilon$ to $r = r_{\max}$. In practice we have taken ϵ such that $|\mathcal{U}(2M + \epsilon)| = \xi \max(|\mathcal{U}|)$, with $\xi = 10^{-3}$. Other values of ξ where tested with similar results. $r_{\max}$ corresponds to the last point of the numerical grid.

IV. TIME DOMAIN DESCRIPTION

In this section we are interested in describing the behavior over time of the radial profiles of resonant states once the harmonic time dependence (5) is relaxed. In particular we are interested in the half-lifetime of the configuration. To proceed, we solve the Klein-Gordon equation in the time domain using the ingoing Kerr-Schild coordinate system. These coordinates are more convenient for numerical analysis because a constant-time hypersurface is nonsingular and horizon penetrating. This characteristic is important in order to impose convenient boundary conditions.

The relation between the Kerr-Schild and Boyer-Lindquist coordinates is given through the time transformation

$$\tilde{t} = t + (r^* - r), \tag{15}$$

where r^* is the tortoise coordinate defined above. In these coordinates, the Schwarzschild metric takes the form

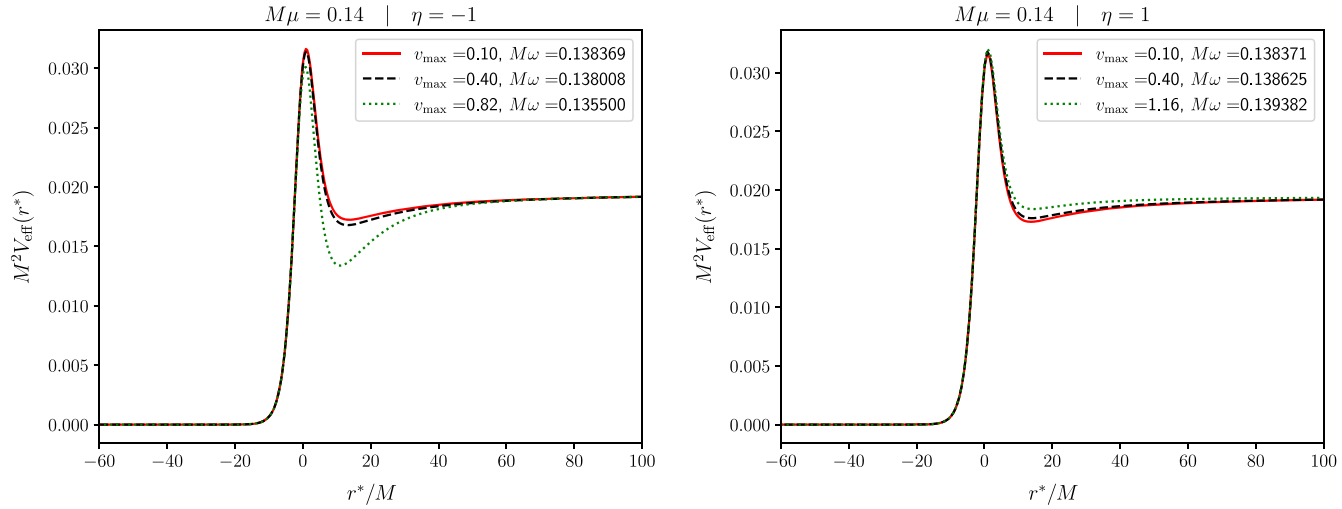

FIG. 11. Effective potential for the fundamental states for different values of $v_{\max}$ in tortoise coordinates. The depth of the potential well increases as $v_{\max}$ grows for $\eta = -1$ and decreases for $\eta = +1$.

$$ds^2 = -\left(1 - \frac{2M}{r}\right)d\tilde{t}^2 + 4\frac{M}{r}dr d\tilde{t} + \left(1 + \frac{2M}{r}\right)dr^2 + r^2(d\theta^2 + \sin^2\theta d\varphi). \tag{16}$$

In terms of Arnowit-Desser-Misner (ADM) variables, see [50] for an introduction, the lapse function α, the shift vector β^r, and the induced 3-metric can be read from Eq. (16) as

$$\alpha = \sqrt{\frac{r}{r+2M}}, \qquad \beta^r = \frac{2M}{2M+r}, \qquad \gamma_{rr} = 1 + \frac{2M}{r}. \tag{17}$$

The complex scalar field can be split into two real scalar fields according to $\Phi = \phi_R + i\phi_I$. The resulting Klein-Gordon equation for Φ can be written as a coupled system,

$$\nabla_\alpha \nabla^\alpha \phi_R = \mu^2 \phi_R + \eta\lambda|\Phi|^2\phi_R,$$
$$\nabla_\alpha \nabla^\alpha \phi_I = \mu^2 \phi_I + \eta\lambda|\Phi|^2\phi_I, \tag{18}$$

where $|\Phi|^2 = \phi_R^2 + \phi_I^2$. In order to solve numerically the system Eq. (18), in the background metric of Eq. (16) and assuming spherical symmetry, we introduce the auxiliary first-order functions

$$\psi_j = \partial_r \phi_j \qquad \pi_j = \alpha^2(\partial_t \phi_j - \beta^r \psi_j), \tag{19}$$

where we have drop the tilde in the time coordinate and $j = \{R, I\}$. The system [Eq. (18)] is thus equivalent to the following evolution equations for ϕ_j, π_j, and ψ_j

$$\partial_t \phi_j = \frac{r}{r+2M}\left(\pi_j + \frac{2M}{r}\psi_j\right),$$
$$\partial_t \psi_j = \frac{2M}{2M+r}\partial_r \psi_j + \frac{r}{2M+r}\partial_r \pi_j + \frac{2M}{(2M+r)^2}(\pi_j - \psi_j),$$
$$\partial_t \pi_j = \frac{1}{2M+r}(2M\pi_j + r\psi_j) + \frac{2M}{(2M+r)^2}(\psi_j - \pi_j) + \frac{2}{r(2M+r)}(r\psi_j + 2M\pi_j) - \phi_j(\mu^2 + \eta\lambda|\Phi|^2). \tag{20}$$

As a diagnostic quantity we use the total energy of the scalar field that in Kerr-Schild coordinates is written as

$$E = 4\pi \int \rho(r)\alpha r^2 dr, \tag{21}$$

where

$$\rho(r) = \frac{1}{2}\left(\alpha^2|\pi|^2 + 2\beta^r(\pi_R\psi_R + \pi_I\psi_I) + \gamma^{rr}|\psi|^2 + \mu^2|\Phi|^2 + \frac{1}{2}\lambda|\Phi|^4\right). \tag{22}$$

The evolution equations for the radial components were solved with the $(1 + 1)$-dimensional PDE solver described in [51] and used in several scenarios [52,53]. The time evolution is done via the method of lines with a third-order total variation diminishing Runge-Kutta algorithm. The spatial derivatives are approximated with a second-order symmetric finite-difference stencil. A standard fourth-order dissipation term was added in order to guarantee the stability of the scheme. The evolution scheme is complemented by imposing an outgoing-wave boundary condition.

A. Initial data: Resonant modes

One may want to evolve directly a resonant state constructed in the frequency domain as described above in order

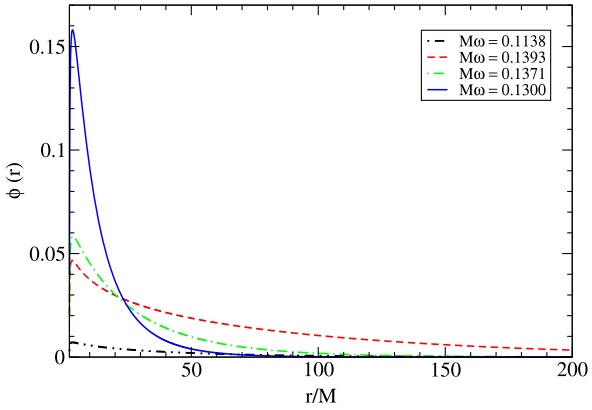

FIG. 12. The initial scalar field profiles correspond to regularized resonant states for configurations with $M\mu = 0.14$. Initially only the real part is different from zero. States with frequencies $\omega = 0.13837$ and $\omega = 0.1371$ are in the weak self-interaction regime with $\eta = +1$ and $\eta = -1$, while states with $\omega = 0.13930$ and $\omega = 0.1300$ are in the strong self-interaction regime with $\eta = +1$ and $\eta = -1$, respectively.

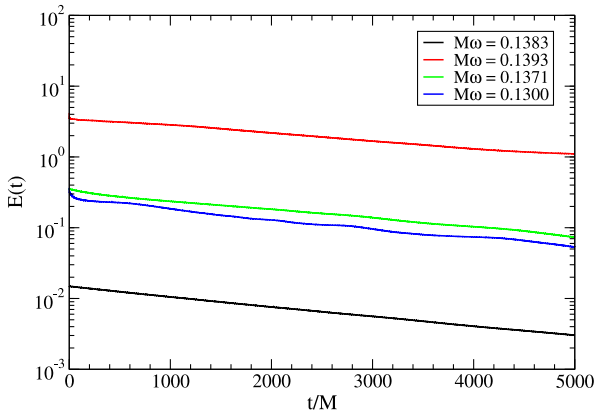

FIG. 13. Energy of the scalar-field states Eq. (21) for $M\mu = 0.14$. The vertical axis is presented in log scale and the properties of the configurations are summarized in Table II. After an initial decay, the energy decays exponentially in time. The rate of decay s, is shown in the last column of Table II.

to determine the time rate of decay; however, those states diverge at the horizon. In order to use the radial function of resonant states as initial data we employ a regularization procedure as described in [37] to mimic a quasiresonant state and smooth its behavior in the region close the horizon. Such procedure allows us to set an initial data close enough to the resonant states found in previous sections. We have used as initial data at $t = 0$ the radial profile of the field $\phi = \frac{u(r)}{r}$, obtained in Sec. III with $M\mu = 0.14$ as

$$\phi_R(0,r) = \phi(r), \qquad \phi_I(0,r) = 0,$$
$$\pi_R(0,r) = \alpha^2\beta^r\partial_r\phi(r), \qquad \pi_I(0,r) = \alpha^2\omega\phi(r), \quad (23)$$

that correspond to the time-harmonic behavior given by Eq. (5). For our analysis we consider states in both weak and strong self-interacting regimes. Figure 12 shows the initial radial distribution $\phi(r)$ with $\eta = +1$ and $\eta = -1$.

As a result of the evolution, the scalar field presents an oscillating behavior and a slow rate of decay. By measuring the field amplitude at a fixed point $r = r_1$ one obtains a time series for the amplitude at that point for both, real and imaginary part. We may thus perform a Fast Fourier Transform to obtain the frequency of oscillation. The power spectrum obtained from the time evolution, shows that both components of the field oscillate with a frequency that corresponds to the frequency obtained in Sec. III. In Fig. 13 we plot the total energy of the scalar configuration as a function of time $E(t)$, defined in Eq. (21). Figure 13 shows that the decay rate of energy is exponential after an initial transient state. We assume that the energy has the form the form $E(t) \sim \exp(-st)$ and perform a linear fit of $\ln(E(t)/E_0)$ with t in order to find the value of the rate of s. The half-lifetime, of the configuration is thus given by $t_{1/2}/M = \ln(2)/s$. We have further considered resonant modes with other values of the coupling $M\mu < 1/4$ and compute the rate of decay of the energy. The results are summarized in Table II. Despite the fact the initial morphology of the scalar-field state is different for configurations with $\eta = +1$ and $\eta = -1$, the rate of decay is of the same order of magnitude for a given value of $M\mu$. We conclude that the effect of λ on the rate of decay is subdominant as compared with the effect of $M\mu$. Notice however, that the effective size of the modes with $\eta = +1$ and large enough values of λ is slightly larger than the noninteracting case, thus if the leaking rate is of the same order of magnitude in both cases, self-interacting clouds will last longer since the initial distribution in the interacting case is larger. Values of the boson mass μ motivated by dark matter scalar field models

TABLE II. Parameters of the quasiresonant states used in the evolution. The last column corresponds to the slope of the line $\ln(E(t)/E_0) = -st$ in Fig. 13. The error reported correspond to the error from the linear fit.

$M\mu$	$M\omega$	$v_{\max}$	Regime	η	s
0.12	0.1192	0.4548	Weak	+1	$1.16 \pm 0.03 \times 10^{-4}$
0.12	0.1196	1.125	Strong	+1	$8.97 \pm 0.13 \times 10^{-5}$
0.12	0.1180	0.6795	Weak	−1	$1.2 \pm 0.05 \times 10^{-4}$
0.12	0.1100	0.9695	Strong	−1	$1.97 \pm 0.02 \times 10^{-4}$
0.14	0.13837	0.1000	Weak	+1	$3.20 \pm 0.05 \times 10^{-4}$
0.14	0.13930	1.050	Strong	+1	$2.70 \pm 0.07 \times 10^{-4}$
0.14	0.1371	0.6192	Weak	−1	$3.03 \pm 0.07 \times 10^{-4}$
0.14	0.1300	0.9158	Strong	−1	$3.27 \pm 0.07 \times 10^{-4}$
0.16	0.1580	0.4725	Weak	+1	$7.05 \pm 0.05 \times 10^{-4}$
0.16	0.1590	1.102	Strong	+1	$4.41 \pm 0.06 \times 10^{-4}$
0.16	0.1560	0.5564	Weak	−1	$6.93 \pm 0.06 \times 10^{-4}$
0.16	0.1500	0.8580	Strong	−1	$5.45 \pm 0.10 \times 10^{-4}$
0.18	0.1780	0.8232	Weak	+1	$1.41 \pm 0.05 \times 10^{-3}$
0.18	0.1790	1.440	Strong	+1	$5.85 \pm 0.05 \times 10^{-4}$
0.18	0.1750	0.4608	Weak	−1	$1.45 \pm 0.05 \times 10^{-3}$
0.18	0.1700	0.7803	Strong	−1	$9.67 \pm 0.05 \times 10^{-4}$

correspond to $\hbar\mu \sim 10^{-24}$ eV, and for a black hole with mass $M \sim 10^8 M_\odot$, the gravitational coupling is of the order of $M\mu \sim 10^{-6}$. This value is slightly smaller than the ones considered in this work, such small values cannot be reached due to the limitations of the numerical integration. However, if we extrapolate our findings as done in Ref. [38] resonant modes may last about 10^9 years.

V. CONCLUDING REMARKS

In this paper we studied the role played by the self-interaction in quasiresonant states of test scalar fields around a Schwarzschild black hole. We assumed that self-interaction is mediated by a term $\sim\lambda|\Phi|^4$ and investigated the properties of the field distribution that forms in the vicinity of black holes in the case of both attractive and repulsive self-interactions. We characterized these cases by means of a parameter η, leaving the parameter λ as a nonnegative quantity. We rewrite the Klein-Gordon equation in terms of a function $v(r)$, allowing us to eliminate the explicit dependence in λ and solve it numerically. With this function one can characterize each solution with its amplitude in the near- and far-horizon regions. We focus our analysis on the resonant modes, which are exponentially decaying solutions at infinity concentrated well outside the event horizon. Furthermore, like in the noninteracting case, resonant modes posses a definite frequency of oscillation.

The first conclusion that can be drawn regarding the role of self-interaction in resonant states is the fact that the values of the discrete frequencies change with respect to the noninteracting case. For $\eta = -1$ the frequency decreases and for $\eta = +1$ it increases compared with the corresponding values of the frequencies without self-interaction.

We have found that in the presence of interactions the size and distribution of the scalar field changes depending on the value of λ. In the regime of strong self-interaction with $\eta = +1$ the size of the resonant scalar cloud distribution increases considerably and the scalar field tends to concentrate more in a region far from the horizon as compared to the case with no self-interaction. Even more, we have found that for large enough values of λ, resonant solutions do not exist. Regarding the self-interaction with $\eta = -1$, the field concentrates closer the horizon with almost no change in size. In this way, we can conclude that, for $\eta = +1$ and large self-interaction the size of the distribution is significantly larger than the $\eta = -1$ and the noninteracting cases.

From a classical perspective this happens because the particles of the configuration tend to concentrate outside the horizon while gravity and attractive self-interactions tend to shrink the configuration towards the black hole. We further investigate the lifetime of resonant states by means of a numerical-time evolution. We found that despite the important role played by the self-interaction in the spatial distribution of the scalar field around the black hole, its role in the lifetime is negligible as compared to the effect of the mass term. In the scenario described in this work we focus on the regime where self-interaction dominates over self-gravitation effects and the parameter λ entered in the equations as a global scale. However, when the spacetime reacts to the presence of the scalar field, the term with λ enters explicitly on the energy density and thus a stronger effect on the properties of the whole configuration is found. A further study, considering the backreaction of the spacetime is under way.

ACKNOWLEDGMENTS

We would like to acknowledge the anonymous referee for the constructive comments and insights which substantially helped to improve the manuscript. This work was partially supported by the CONACyT Network Projects No. 376127 "Sombras, lentes y ondas gravitatorias generadas por objetos compactos astrofísicos", and No. 304001 "Estudio de campos escalares con aplicaciones en cosmología y astrofísica", by DGAPA-UNAM through Grant No. IN105 920 and by the European Union's Horizon 2020 research and innovation (RISE) Program H2020-MSCA-RISE-2017 (Grant No. FunFiCO-777740). A. A. and V. J. acknowledge financial support from CONACyT graduate grant program.

APPENDIX: MULTIFIELD CONFIGURATIONS

In Refs. [54] self-gravitating spherically symmetric multifield configurations were considered. In these configurations an spherically symmetric tensor can be constructed assuming that the amplitudes of the constituents fields are the equal. The Lagrangian for $N = 2\ell + 1$ self-interacting complex scalar fields with a $U(N)$ symmetry is

$$\mathcal{L}_\phi = -\sum_{i=1}^{N}\left(\nabla_\mu\Phi_i\nabla^\mu\Phi_i^* + \mu^2|\Phi_i|^2 + \frac{1}{2}\lambda|\Phi_i|^2\sum_{j=1}^{N}|\Phi_j|^2\right), \tag{A1}$$

where each field is given by

$$\Phi_m(t,r,\theta,\varphi) = \frac{u(r)}{r}e^{i\omega t}Y^{\ell m}(\theta,\varphi)\sqrt{\frac{4\pi}{2\ell+1}}. \tag{A2}$$

with $m = i - \ell - 1$. Using this ansatz for the fields Φ_m, the resulting Klein-Gordon equation for each of the $2\ell + 1$ fields is the same for all of them and is identical to Eq. (6) under the substitution

$$\mathcal{U}(r) \to \mathcal{U}(r) + \frac{\ell(\ell+1)}{r^2}. \tag{A3}$$

[1] Wayne Hu, Rennan Barkana, and Andrei Gruzinov, Fuzzy Cold Dark Matter: The Wave Properties of Ultralight Particles, Phys. Rev. Lett. **85**, 1158 (2000).

[2] Tonatiuh Matos, Francisco Siddhartha Guzman, and L. Arturo Urena-Lopez, Scalar field as dark matter in the universe, Classical Quantum Gravity **17**, 1707 (2000).

[3] Tonatiuh Matos and L. Arturo Urena-Lopez, Quintessence and scalar dark matter in the universe, Classical Quantum Gravity **17**, L75 (2000).

[4] Tonatiuh Matos and L. Arturo Urena-Lopez, A further analysis of a cosmological model of quintessence and scalar dark matter, Phys. Rev. D **63**, 063506 (2001).

[5] P. Sikivie and Q. Yang, Bose-Einstein Condensation of Dark Matter Axions, Phys. Rev. Lett. **103**, 111301 (2009).

[6] Y. V. Stadnik and V. V. Flambaum, Can Dark Matter Induce Cosmological Evolution of the Fundamental Constants of Nature?, Phys. Rev. Lett. **115**, 201301 (2015).

[7] Y. V. Stadnik and V. V. Flambaum, Improved limits on interactions of low-mass spin-0 dark matter from atomic clock spectroscopy, Phys. Rev. A **94**, 022111 (2016).

[8] Lam Hui, Jeremiah P. Ostriker, Scott Tremaine, and Edward Witten, Ultralight scalars as cosmological dark matter, Phys. Rev. D **95**, 043541 (2017).

[9] R. D. Peccei and Helen R. Quinn, *CP* Conservation in the Presence of Instantons, Phys. Rev. Lett. **38**, 1440 (1977).

[10] Asimina Arvanitaki, Savas Dimopoulos, Sergei Dubovsky, Nemanja Kaloper, and John March-Russell, String axiverse, Phys. Rev. D **81**, 123530 (2010).

[11] Asimina Arvanitaki and Sergei Dubovsky, Exploring the string axiverse with precision black hole physics, Phys. Rev. D **83**, 044026 (2011).

[12] P. Sikivie, Axion Dark Matter Detection using Atomic Transitions, Phys. Rev. Lett. **113**, 201301 (2014); **125**, 029901(E) (2020).

[13] David J. E. Marsh and Joe Silk, A model for halo formation with axion mixed dark matter, Mon. Not. R. Astron. Soc. **437**, 2652 (2014).

[14] N. K. Porayko and K. A. Postnov, Constraints on ultralight scalar dark matter from pulsar timing, Phys. Rev. D **90**, 062008 (2014).

[15] Hsi-Yu Schive, Tzihong Chiueh, and Tom Broadhurst, Cosmic structure as the quantum interference of a coherent dark wave, Nat. Phys. **10**, 496 (2014).

[16] David J. E. Marsh and Ana-Roxana Pop, Axion dark matter, solitons and the cusp-core problem, Mon. Not. R. Astron. Soc. **451**, 2479 (2015).

[17] David J. E. Marsh, Axion cosmology, Phys. Rep. **643**, 1 (2016).

[18] Tonatiuh Matos, Argelia Bernal, and Dario Núñez, Flat central density profiles from scalar field dark matter halo, Rev. Mex. Astron. Astrofis. **44**, 149 (2008).

[19] Tonatiuh Matos and L. Arturo Urena-Lopez, Flat rotation curves in scalar field galaxy halos, Gen. Relativ. Gravit. **39**, 1279 (2007).

[20] B. P. Abbott *et al.*, GWTC-1: A Gravitational-Wave Transient Catalog of Compact Binary Mergers Observed by LIGO and Virgo during the First and Second Observing Runs, Phys. Rev. X **9**, 031040 (2019).

[21] B. P. Abbott *et al.*, Binary black hole population properties inferred from the first and second observing runs of Advanced LIGO and Advanced Virgo, Astrophys. J. Lett. **882**, L24 (2019).

[22] R. Abbott *et al.*, GWTC-2: Compact Binary Coalescences Observed by LIGO and Virgo During the First Half of the Third Observing Run, Phys. Rev. X **11**, 021053 (2021).

[23] R. Abbott *et al.*, GWTC-3: Compact Binary Coalescences Observed by LIGO and Virgo During the Second Part of the Third Observing Run, 2021.

[24] Kazunori Akiyama *et al.*, First M87 event horizon telescope results. I. The shadow of the supermassive black hole, Astrophys. J. Lett. **875**, L1 (2019).

[25] Kazunori Akiyama *et al.*, First M87 event horizon telescope results. VI. The shadow and mass of the central black hole, Astrophys. J. Lett. **875**, L6 (2019).

[26] Kazunori Akiyama *et al.*, First sagittarius A* event horizon telescope results. I. The shadow of the supermassive black hole in the center of the Milky Way, Astrophys. J. Lett. **930**, L12 (2022).

[27] T. Damour and R. Ruffini, Black hole evaporation in the Klein-Sauter-Heisenberg-Euler formalism, Phys. Rev. D **14**, 332 (1976).

[28] T. J. M. Zouros and D. M. Eardley, Instabilities of massive scalar perturbations of a rotating black hole, Ann. Phys. (N.Y.) **118**, 139 (1979).

[29] S. Detweiler, Klein-Gordon equation and rotating black holes, Phys. Rev. D **22**, 2323 (1980).

[30] A. B. Gaina and O. B. Zaslavskii, On quasilevels in the gravitational field of a black hole, Classical Quantum Gravity **9**, 667 (1992).

[31] Vitor Cardoso and Shijun Yoshida, Superradiant instabilities of rotating black branes and strings, J. High Energy Phys. 07 (2005) 009.

[32] Anthony Lasenby, Chris Doran, Jonathan Pritchard, Alejandro Caceres, and Sam Dolan, Bound states and decay times of fermions in a Schwarzschild black hole background, Phys. Rev. D **72**, 105014 (2005).

[33] Julien Grain and A. Barrau, Quantum bound states around black holes, Eur. Phys. J. C **53**, 641 (2008).

[34] Sam R. Dolan, Instability of the massive Klein-Gordon field on the Kerr spacetime, Phys. Rev. D **76**, 084001 (2007).

[35] Helvi Witek, Vitor Cardoso, Akihiro Ishibashi, and Ulrich Sperhake, Superradiant instabilities in astrophysical systems, Phys. Rev. D **87**, 043513 (2013).

[36] J. Barranco, A. Bernal, J. C. Degollado, A. Diez-Tejedor, M. Megevand, M. Alcubierre, D. Núñez, and O. Sarbach, Schwarzschild Black Holes Can Wear Scalar Wigs, Phys. Rev. Lett. **109**, 081102 (2012).

[37] J. Barranco, A. Bernal, J. C. Degollado, A. Diez-Tejedor, M. Megevand, M. Alcubierre, D. Núñez, and O. Sarbach, Are black holes a serious threat to scalar field dark matter models?, Phys. Rev. D **84**, 083008 (2011).

[38] J. Barranco, A. Bernal, J. C. Degollado, A. Diez-Tejedor, M. Megevand, M. Alcubierre, D. Núñez, and O. Sarbach, Schwarzschild scalar wigs: Spectral analysis and late time behavior, Phys. Rev. D **89**, 083006 (2014).

[39] M. Colpi, S. L. Shapiro, and I. Wasserman, Boson Stars: Gravitational Equilibria of Self-Interacting Scalar Fields, Phys. Rev. Lett. **57**, 2485 (1986).

[40] Steven L. Liebling and Carlos Palenzuela, Dynamical boson stars, Living Rev. Relativity **15**, 6 (2012).

[41] Jose P. S. Lemos and Oleg B. Zaslavskii, Black hole mimickers: Regular versus singular behavior, Phys. Rev. D **78**, 024040 (2008).
[42] F. Siddhartha Guzman, Accretion disc onto boson stars: A way to supplant black holes candidates, Phys. Rev. D **73**, 021501 (2006).
[43] Eckehard W. Mielke and Franz E. Schunck, Boson stars: Alternatives to primordial black holes?, Nucl. Phys. **B564**, 185 (2000).
[44] D. F. Torres, S. Capozziello, and G. Lambiase, A supermassive boson star at the galactic center?, Phys. Rev. D **62**, 104012 (2000).
[45] Pau Amaro-Seoane, Juan Barranco, Argelia Bernal, and Luciano Rezzolla, Constraining scalar fields with stellar kinematics and collisional dark matter, J. Cosmol. Astropart. Phys. 11 (2010) 002.
[46] Bohua Li, Tanja Rindler-Daller, and Paul R. Shapiro, Cosmological constraints on Bose-Einstein-condensed scalar field dark matter, Phys. Rev. D **89**, 083536 (2014).
[47] Abril Suárez and Pierre-Henri Chavanis, Cosmological evolution of a complex scalar field with repulsive or attractive self-interaction, Phys. Rev. D **95**, 063515 (2017).
[48] Eréndira Gutiérrez-Luna, Belen Carvente, Víctor Jaramillo, Juan Barranco, Celia Escamilla-Rivera, Catalina Espinoza, Myriam Mondragón, and Darío Núñez, Scalar field dark matter with two components: Combined approach from particle physics and cosmology, Phys. Rev. D **105**, 083533 (2022).
[49] Alejandro Escorihuela-Tomàs, Nicolas Sanchis-Gual, Juan Carlos Degollado, and José A. Font, Quasistationary solutions of scalar fields around collapsing self-interacting boson stars, Phys. Rev. D **96**, 024015 (2017).
[50] A. Corichi and D. Núñez, Introduction to the ADM formalism, Rev. Mex. Fis. **37**, 720 (1991).
[51] Dario Núñez, Juan Carlos Degollado, and Claudia Moreno, Gravitational waves from scalar field accretion, Phys. Rev. D **84**, 024043 (2011).
[52] Juan Carlos Degollado and Carlos A. R. Herdeiro, Time evolution of superradiant instabilities for charged black holes in a cavity, Phys. Rev. D **89**, 063005 (2014).
[53] Claudia Moreno, Juan Carlos Degollado, Darío Núñez, and Carlos Rodríguez-Leal, Gravitational and electromagnetic perturbations of a charged black hole in a general gauge condition, Particles **4**, 106 (2021).
[54] Ignacio Olabarrieta, Jason F. Ventrella, Matthew W. Choptuik, and William G. Unruh, Critical behavior in the gravitational collapse of a scalar field with angular momentum in spherical symmetry, Phys. Rev. D **76**, 124014 (2007).